



# Optical properties and simulated x-ray near edge spectra for $\text{Y}_2\text{O}_2\text{S}$ and Er doped $\text{Y}_2\text{O}_2\text{S}$



Nicholas Dimakis<sup>a,\*</sup>, Eric Baldemar Jr. Rodriguez<sup>b</sup>, Kofi Nketia Ackaah-Gyasi<sup>c</sup>, Madhab Pokhrel<sup>a</sup>

<sup>a</sup> Department of Physics and Astronomy, University of Texas Rio Grande Valley, Edinburg 78539, USA

<sup>b</sup> Department of Mechanical Engineering, University of Texas Rio Grande Valley, Edinburg 78539, USA

<sup>c</sup> Department of Computer Science, University of Texas Rio Grande Valley, Edinburg 78539, USA

## ARTICLE INFO

### Keywords:

DFT  
GW  
 $\text{Y}_2\text{O}_2\text{S}$   
Er  
Intraband transitions

## ABSTRACT

The electronic and optical properties of  $\text{Y}_2\text{O}_2\text{S}$  and its  $\text{Er}^{+3}$  doped counterparts at various concentrations are analyzed using density functional theory (DFT) and simulated x-ray near edge (XANES) spectra. Our simulations are complemented by absorption experiments, which show  $\text{Y}_2\text{O}_2\text{S}:\text{Er}^{+3}$  light emissions in the visible and near infrared. These emissions correspond to Er f-f intraband transitions. We use DFT and DFT+U to calculate the band structure of the  $\text{Y}_2\text{O}_2\text{S}$  and its  $\text{Er}^{+3}$  doped counterparts, whereas optical properties are calculated using the independent particle approximation (IPA). The host  $\text{Y}_2\text{O}_2\text{S}$  optical properties are also calculated using the random phase approximation (RPA) and the many-body  $\text{GW}_0$  approximation. Our IPA calculations on the  $\text{Y}_2\text{O}_2\text{S}:\text{Er}^{+3}$  reveal transitions in the energy region of the bandgap, which are absent in the host spectrum. These are assigned to Er f-f intraband transitions in the visible and near infrared, by applying a rigid energy shift. Moreover, XANES calculations at the Er M<sub>5</sub>-edge reveal a pre-edge broad shoulder in the proximity of the Er 4f band, which is also supportive of the f-f intraband transitions.

## 1. Introduction

Rare earth doped materials have unique optical and electrical properties and serve in optoelectronic devices, such as displays [1–3]. Among the rare earth doped materials,  $\text{Y}_2\text{O}_2\text{S}$  serves as a phosphorescent host for doping with Eu [4–6], Er [7,8], Mg, and Ti atoms [5,9].  $\text{Y}_2\text{O}_2\text{S}$  is a wide band semiconductor with an indirect band gap of 4.6–4.8 eV [10–12]. It can be easily synthesized in the laboratory and it has been reported as one of the most efficient upconversion hosts [13]. The  $\text{Y}_2\text{O}_2\text{S}$  reflectivity spectra have been measured by Itoh and Inabe, who used Kramers-Kronig analysis to derive the  $\text{Y}_2\text{O}_2\text{S}$  real and imaginary parts of the frequency-dependent dielectric function and its absorption spectrum [14]. Their calculated  $\text{Y}_2\text{O}_2\text{S}$  bandgap was 6.77 eV and was obtained using the Wannier-Mott model for the energy levels of the exciton. However, this value is considered overestimated [15]. The  $\text{Y}_2\text{O}_2\text{S}$  electronic band structure has been previously calculated using density functional theory (DFT) [7,16], which confirmed that the  $\text{Y}_2\text{O}_2\text{S}$  bandgap is indirect. Li and Ahuja used the full-potential linear muffin-tin orbital method to calculate the  $\text{Y}_2\text{O}_2\text{S}$  electronic structure, its elastic

constants, and its dielectric function [15]. The authors reported the  $\text{Y}_2\text{O}_2\text{S}$  dielectric constant at 5.3, which is close to the corresponding  $\text{La}_2\text{O}_2\text{S}$  experimental value of 4.67 [17].

Among rare earth atoms, erbium (Er) is one of the most studied dopants for its luminescence in the near infrared and visible region [18, 19]. Due to the availability of the 980 nm laser, where ytterbium ( $\text{Yb}^{3+}$ ) has a strong absorption,  $\text{Er}^{3+}$  shows promising, as a center for both Stoke's and anti-Stokes luminescence [20]. Buddhudu and Bryant measured the  $\text{Y}_2\text{O}_2\text{S}:\text{Er}^{+3}$  and  $\text{La}_2\text{O}_2\text{S}:\text{Er}^{+3}$  absorption spectra and identified the Er intraband f-f transitions [21]. Pokhrel et al., used crystal field theory to examine these intraband transitions and correlate them with experimental absorption spectra for  $\text{Y}_2\text{O}_2\text{S}:\text{Er}^{+3}$  at Er concentrations up to 10%. In addition, they reported the band structure for  $\text{Y}_2\text{O}_2\text{S}$  and the density of states (DOS) for both  $\text{Y}_2\text{O}_2\text{S}$  and  $\text{Y}_2\text{O}_2\text{S}:\text{Er}^{+3}$ . However, no correlation between electronic and optical properties was made. In this paper, we have performed a detailed study using various computational methods, such as DFT [22,23], simulated x-ray near edge structure (XANES), and beyond, to correlate electronic band spectra for  $\text{Y}_2\text{O}_2\text{S}:\text{Er}^{+3}$  with frequency-dependent optical properties, such as the

\* Corresponding author.

E-mail address: [Nicholas.dimakis@utrgv.edu](mailto:Nicholas.dimakis@utrgv.edu) (N. Dimakis).

dielectric function, reflectivity, refractive index, and absorption coefficient. XANES is proportional to the imaginary part of the frequency-dependent dielectric function and is used to determine transitions from core and valence states to unfilled and partially filled bound states and to the continuum [24].

Here, our DFT calculations are complemented with experimental absorption spectra for  $\text{Y}_2\text{O}_2\text{S}:\text{Er}^{3+}$ . The electronic structure is calculated using DFT and the Hubbard U DFT+U correction by Liechtenstein et al. [25], for both the host  $\text{Y}_2\text{O}_2\text{S}$  and its doped structures. The computationally expressive hybrid HSE06 functional [26] and the many-body  $\text{GW}_0$  approximation [27] are also used for the bandgap estimation of the  $\text{Y}_2\text{O}_2\text{S}$  host. The  $\text{GW}$  approximation accurately calculates the excitation spectra (i.e., quasiparticle energies), by correctly considering the electron-electron correlation effects [28,29], whereas in the  $\text{GW}_0$  the green function  $G$  is updated till its convergence is obtained self-consistently. We calculate the  $\text{Y}_2\text{O}_2\text{S}$  host optical properties using the independent particle approximation (IPA) [30,31], the random phase approximation (RPA) [32], and the RPA corrected version using  $\text{GW}_0$  for the quasiparticle energies ( $\text{GW}_0+\text{RPA}$ ). RPA and  $\text{GW}_0+\text{RPA}$  are of higher accuracy than IPA but impractical when large supercells are used. The IPA is used for optical properties calculations of the doped  $\text{Y}_2\text{O}_2\text{S}:\text{Er}^{3+}$  to analyze the Er 4f intraband transitions. These intraband transitions are also revealed from the calculated XANES at the Er M<sub>5</sub>-edge, though examination of its pre-edge region.

## 2. Experimental and computational methods

### 2.1. Synthesis and characterization of the host $\text{Y}_2\text{O}_2\text{S}$ and the doped $\text{Y}_2\text{O}_2\text{S}:\text{Er}^{3+}$

#### 2.1.1. Synthesis

The  $\text{Y}_2\text{O}_2\text{S}:\text{x%Er}^{3+}$  ( $x = 0, 3, 7$ , and  $10 \text{ mol\%}$ ) were synthesized using a two-step method. At the first step, the  $\text{Y}_2\text{O}_3:\text{x%Er}^{3+}$  were synthesized using the homogeneous precipitation method [33]. All chemicals were 99.9% pure and were purchased from Sigma-Aldrich.  $\text{Y}(\text{NO}_3)_3 \cdot 0.6 \text{ H}_2\text{O}$  (5 mM) and  $\text{Er}(\text{NO}_3)_3 \cdot 0.6 \text{ H}_2\text{O}$  (1–10 mol% of  $\text{Y}(\text{NO}_3)_3 \cdot 0.6 \text{ H}_2\text{O}$ ) were dissolved in 1.0 M concentrated urea solution set with circulating bath at

90 °C for 3 hrs, upon constant stir. The  $\text{OH}^-$  ions were generated through solubility of urea in water. Additional details on the homogeneous precipitation synthesis method can also be found in past publications [33]. In the second step, the as prepared  $\text{Y}_2\text{O}_3:\text{x%Er}^{3+}$  were sulfureted by using the double crucible method, as reported in the literature [34]. Sulfur powder and the  $\text{Na}_2\text{CO}_3$  and  $\text{K}_3\text{PO}_4$  (Sigma Aldrich, 99.99%) were used as flux. The precursor materials were thoroughly mixed and annealed in a box furnace. The ramp up rate was maintained at 10 °C/min, but the furnace was allowed to cool down naturally after annealing the mixture at 1100 °C for 90 min. Room temperature samples were washed with distilled water and alcohol. The washed powder was dried and grinded for further characterization.

#### 2.1.2. Sample characterization and absorption spectra

Powder x-ray diffraction (XRD) patterns of the  $\text{Y}_2\text{O}_2\text{S}:\text{x%Er}^{3+}$  ( $x = 0, 3, 7$  and  $10$ ) were collected using Bruker 800D x-ray diffractometer with  $\text{CuK}\alpha_1$  radiation ( $\lambda = 0.15,406 \text{ nm}$ ). The XRD data were collected by scanning mode in the  $2\theta$  ranging from 10° to 80° with a scanning step size of 0.04° and a rate of 1.0° min<sup>-1</sup>. The excitation, and emission spectra including lifetime measurements of the  $\text{Y}_2\text{O}_2\text{S}:\text{Er}^{3+}$  powders were measured using an Edinburgh Instruments FLS980 fluorometer system. The absorption spectra were measured in the 300–1700 nm range using the Lamda-9000 UV-VIS-NIR Perkin Elmer spectrophotometer in reflection mode.

## 2.2. Computational modeling and parameters

### 2.2.1. Unit cell and supercell modeling

Fig. 1 shows the  $\text{Y}_2\text{O}_2\text{S}$  unit cell in a triclinic form (space group  $\overline{\text{P}}\bar{3}\text{m}1$ ) and its supercell in cubic form for  $\text{Y}_2\text{O}_2\text{S}$  doped with 9.375%  $\text{Er}^{3+}$  (i.e., 3 Er atoms in the unit cell). This supercell is used for all doped  $\text{Y}_2\text{O}_2\text{S}:\text{Er}^{3+}$  configurations and for the host  $\text{Y}_2\text{O}_2\text{S}$ . Each yttrium atom is coordinated with three oxygens as nearest neighbors, one oxygen as next nearest neighbor, and with three sulfur atoms thereafter. The  $\text{Y}_2\text{O}_2\text{S}$  supercell is built from the triclinic unit cell by using the following transformation matrix

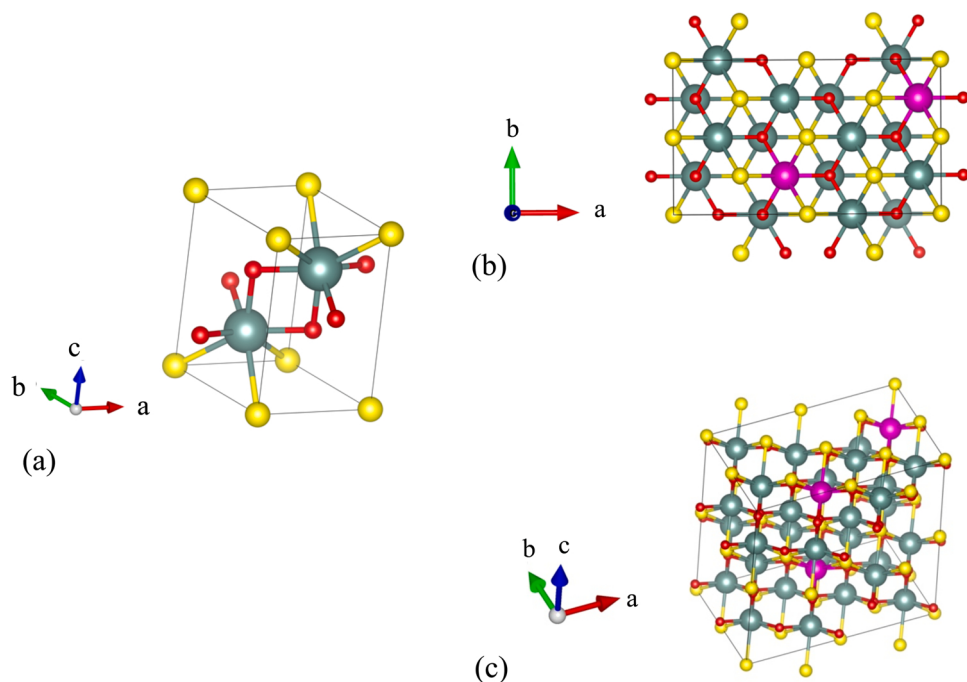


**Fig. 1.** (a) The crystal structure of the  $\text{Y}_2\text{O}_2\text{S}$  unit cell in its triclinic form and (b) and (c) the  $\text{Y}_2\text{O}_2\text{S}:\text{Er}^{3+}$  with 9.375% Er doping in a cubic form after using the transformation of Eq. (1). The thin lines denote the unit cell boundaries. Atoms are colors as follows: Er, Y, O, and S are violet, green, red, and yellow, respectively.

$$T = x \bullet \begin{pmatrix} 1 & 1 & 0 \\ -1 & 1 & 0 \\ 0 & 0 & 1 \end{pmatrix} \Big|_{x=2} \quad (1)$$

and contains 80 atoms. We also use a smaller 10-atom unit cell for the host  $\text{Y}_2\text{O}_2\text{S}$  ( $x = 1$  in Eq. 1), where we calculate optical properties using the IPA, RPA, and  $\text{GW}_0$  methods.

The XANES calculated spectra for the  $\text{Y}_2\text{O}_2\text{S}: \text{Er}^{+3}$  configurations are obtained using clusters of 140 atoms and radius of about 7.9 Å around the absorbing Er atom. For the undoped case, XANES is calculated using the k-space approach [35], and thus a  $\text{Y}_2\text{O}_2\text{S}$  unit cell is used (Fig. 1a).

### 2.2.2. DFT parameters

DFT electronic calculations, optimal geometries, and optical properties of  $\text{Y}_2\text{O}_2\text{S}$  and  $\text{Y}_2\text{O}_2\text{S}$  doped with  $\text{Er}^{+3}$  were performed using the periodic code Vienna Ab initio Simulation Package (VASP) [36–39] under the PAW pseudopotentials [40,41]. The Kohn-Sham equations were solved using the generalized gradient approximation under the Perdew–Burke–Ernzerhof (PBE) functional [42]. We use the D3 semi-empirical correction by Grimme [43], which improves the DFT functionals descriptions for the long-range electron correlations responsible for van der Waals interactions. The kinetic energy cutoff for all calculations was 525 eV. Optimal geometries were obtained by relaxing all atomic positions till the forces on each atom are  $\leq 10^{-4}$  eV/Å. The energy SCF convergence threshold is set at  $10^{-9}$  eV per atom. The Brillouin-zone (BZ) was sampled using the  $4 \times 4 \times 4$  Monkhorst-Pack grid for geometry optimizations and electronic information [44]. Optical properties are calculated using the  $\Gamma$ -centered  $6 \times 6 \times 6$  BZ grid. We also report additional optical properties calculations using the denser  $\Gamma$ -centered  $8 \times 8 \times 8$  grid for the 10-atom  $\text{Y}_2\text{O}_2\text{S}$  unit cell. Fig. 2 shows the BZ path used here for electronic band structure calculations. The band structure and the DOS are performed with both DFT and DFT+U calculations [25], the latter leads to a larger bandgap for  $\text{Y}_2\text{O}_2\text{S}$ , which is closer to experimental findings. For the 10-atom  $\text{Y}_2\text{O}_2\text{S}$  host structure, the bandgap is calculated by both the HSE06 and the  $\text{GW}_0$  approximation, which are both impractical to be used with the 80 atoms supercells. Additional grids are used for the evaluation of the augmentation charges, thus enhancing the accuracy of our calculations. The valance electron configurations for Y, O, S, and Er are  $4s^24p^65s^14d^2$ ,  $2s^22p^4$ ,  $3s^23p^4$ , and  $5s^25p^64f^{11}5d^16s^2$ , respectively.

The Bader Charge Analysis code [45–48] was used to obtain Bader-type ion charges [49] for the configurations of this work. This code, developed by Henkelman and co-workers, partitions the charge density grid into Bader-type volumes and scales linearly with the number of grid points. Thus, this code can be used for large systems.

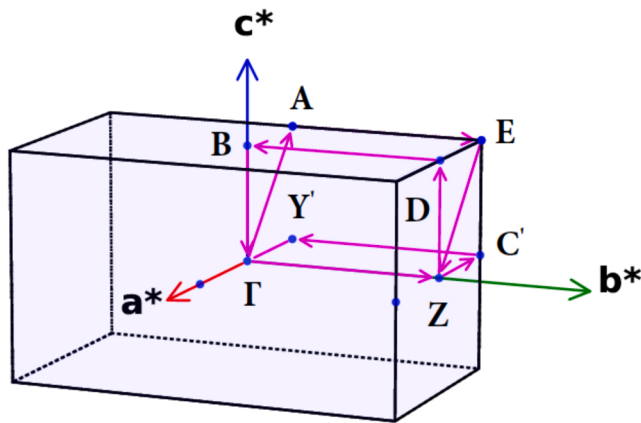


**Fig. 2.** The first BZ of the  $\text{Y}_2\text{O}_2\text{S}$  cubic lattice with the symmetry points as follows:  $\Gamma$ , Z, D, B, A, E, Y', and C' are found at  $(0, 0, 0)$ ,  $(0, \frac{1}{2}, 0)$ ,  $(0, \frac{1}{2}, \frac{1}{2})$ ,  $(-\frac{1}{2}, \frac{1}{2}, \frac{1}{2})$ ,  $(-\frac{1}{2}, 0, 0)$ , and  $(-\frac{1}{2}, \frac{1}{2}, 0)$ , respectively. The BZ path used  $\Gamma$ -Z-D-B-A-E-Z-C'-Y'- $\Gamma$  is shown by purple arrows.

### 2.2.3. Optical properties

The frequency-dependent dielectric function is written as

$$\epsilon(\omega) = \epsilon_R(\omega) + i\epsilon_I(\omega) \quad (2)$$

where  $\epsilon_R(\omega)$  and  $\epsilon_I(\omega)$  are the dielectric function real and imaginary parts, respectively. The refractive index  $n(\omega)$ , the extinction coefficient  $\kappa(\omega)$ , the absorption coefficient  $\alpha(\omega)$ , and the reflectivity  $R(\omega)$  are given by

$$n(\omega) = \left( \frac{(\epsilon_R(\omega)^2 + \epsilon_I(\omega)^2)^{1/2} + \epsilon_R(\omega)}{2} \right)^{1/2} \quad (3)$$

$$\kappa(\omega) = \left( \frac{(\epsilon_R(\omega)^2 + \epsilon_I(\omega)^2)^{1/2} - \epsilon_R(\omega)}{2} \right)^{1/2} \quad (4)$$

$$\alpha(\omega) = \frac{2\omega}{c} \kappa(\omega) \quad (5)$$

$$R(\omega) = \frac{(n(\omega) - 1)^2 + k(\omega)^2}{(n(\omega) + 1)^2 + k(\omega)^2} \quad (6)$$

RPA and  $\text{GW}_0+\text{RPA}$  calculations include local field effects at the Hartree level [50].

### 2.2.4. XANES parameters

XANES is calculated using the FEFF 10 [51–53] code through real space Green functions under self-consistent calculations, which account for more accurate chemical shifts. All our calculations consider full multiple scattering. The exchange interaction was accounted using the Hedin-Lundqvist pseudopotential [54] and the absorbing atom core hole was treated using the RPA method. We also use FEFF 10 to calculate projected DOS, which shows the orbital contribution for the x-ray edge transitions. For FEFF calculated DOS, the Lorentzian parameter of 0.1 eV half-width was used.

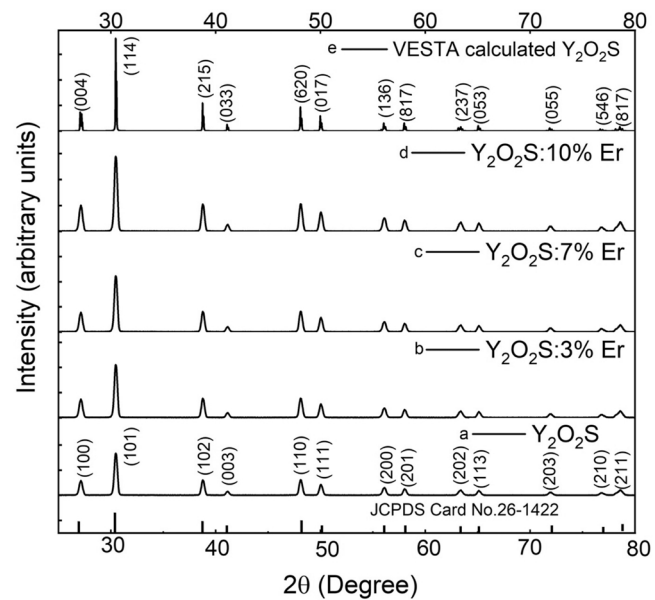


**Fig. 3.** XRD spectra with the corresponding Miller indices. (a) as synthesized  $\text{Y}_2\text{O}_2\text{S}$  and  $\text{Er}^{3+}$  doped samples, (b) 3%, (c) 7%, (d) 10%  $\text{Er}^{+3}$ , and (e) VESTA calculated spectra for the supercell structure of Fig. 1b.

### 3. Results and discussion

#### 3.1. Structural information for the host $\text{Y}_2\text{O}_2\text{S}$ and the $\text{Y}_2\text{O}_2\text{S}:\text{Er}^{+3}$

**Fig. 3** shows the XRD patterns for the as synthesized  $\text{Y}_2\text{O}_2\text{S}:x\%\text{Er}^{+3}$  ( $x = 0, 3, 7, 10 \text{ mol\%}$ ) in comparison with the JCPDS card no.:26–1612 and the VESTA calculated spectra for  $\text{Y}_2\text{O}_2\text{S}:\text{Er}^{+3}$  at 9.375% doping. The Miller indices for the calculated spectra correspond to the supercell structure of **Fig. 1b**, which is cubic, whereas the ones for the experimental spectra refer to the triclinic phase. The VESTA calculated XRD spectra for the  $\text{Y}_2\text{O}_2\text{S}$  using the triclinic configuration of **Fig. 1a** can be found in **Fig. S1**, where its Miller indices are in excellent agreement with the experimental XRD spectra of **Fig. 3**. There is a peak alignment among all XRD spectra, and no additional phases are observed (**Fig. 3, S1**). This shows that the  $\text{Y}_2\text{O}_2\text{S}:\text{Er}^{+3}$  have the same crystal phase as the corresponding host  $\text{Y}_2\text{O}_2\text{S}$  and that no significant changes are observed in the Y-O and Y-S distances due to doping with Er. Moreover, our work authenticates the current synthesis approach of  $\text{Y}_2\text{O}_2\text{S}$  and  $\text{Y}_2\text{O}_2\text{S}:\text{Er}^{+3}$  phosphors.

**Table 1** shows our DFT calculated lattice parameters and bandgaps for the  $\text{Y}_2\text{O}_2\text{S}$  and the  $\text{Y}_2\text{O}_2\text{S}:\text{Er}^{+3}$ , at various Er concentrations. Our calculated lattice parameters for  $\text{Y}_2\text{O}_2\text{S}$  well agree with past experimental and computational reports. For  $\text{Y}_2\text{O}_2\text{S}$ , our calculated Y-O distances are 2.26 Å for three Y-O distances and 2.29 Å for one Y-O distance, whereas the Y-S distance is 2.868 Å, in agreement with Pokhrel et al. [7]. For 9.375% Er doping, which is the maximum doping used at the computational part of this work, the Er-O and Er-S distances are 2.276 Å (three Er-O distances) and 2.316 Å (one Er-O distance) and 2.851 Å, respectively. These distances are about the same as the Y-O and Y-S distances, in agreement with the XRD results (**Fig. 3**).

#### 3.2. Electronic band structure, densities of states, and charge transfer calculations

**Fig. 4** shows the electronic band structure and the total DOS and per orbital for the host  $\text{Y}_2\text{O}_2\text{S}$  and its doped counterparts at 3.175%, 6.25%, and 9.375% Er concentrations. In addition, **Fig. 4b** shows electron excitations, which correspond to excitations deducted from the optical properties' calculations. **Fig. S2** shows the same information as **Fig. 4** (without excitations) but under the DFT+U calculations, with  $U_d(\text{Y}) = 12 \text{ eV}$  and  $J_d(\text{Y}) = 1 \text{ eV}$ . The U and J values were selected so that the calculated bandgap is closer to the experimentally accepted values of 4.4–4.6 eV [10–12]. The U values are larger for 4d than 5d elements due to the higher electron localization for smaller quantum numbers [55]. Additional calculations showed that further increase of the  $U_d(\text{Y})$  parameter minimally affected the bandgap. Our DFT calculations show

**Table 1**

Structural parameters and bandgaps ( $E_g$ ) for  $\text{Y}_2\text{O}_2\text{S}$  and its  $\text{Er}^{+3}$ -doped counterparts. Values in parenthesis refer to experimental and computational data from the literature.

Structure	Lattice Parameters		$E_g$ (eV)
	a (Å)	c (Å)	
$\text{Y}_2\text{O}_2\text{S}$	3.7826 (3.7910) <sup>c</sup> [14]	6.5689 (6.596) <sup>c</sup> [14]	3.01; 3.80 <sup>a</sup> ; 3.94 <sup>b</sup> ; 5.30 <sup>c</sup> (4.6[11], 4.8[10], 6.77 [14]) <sup>d</sup>
$\text{Y}_2\text{O}_2\text{S}: 3.125\% \text{ Er}^{+3}$	(3.750)[12] <sup>e</sup> (3.7611)[7] <sup>f</sup> (3.751 <sup>e</sup> ; 3.816 <sup>f</sup> )	(6.525)[12] <sup>e</sup> (6.4770)[7] <sup>f</sup> (6.527 <sup>e</sup> ; 6.640 <sup>f</sup> )	(2.61)[12] <sup>e</sup> (2.979)[7] <sup>f</sup> (2.8 <sup>e</sup> ; 3.00 <sup>f</sup> )[15]
6.25% $\text{Er}^{+3}$	3.7820	6.5696	2.73, 0.13; 2.92 <sup>a</sup> , 0.13 <sup>a</sup>
9.375% $\text{Er}^{+3}$	3.7815 3.7807	6.5703 6.5707	2.75, 0.18; 2.96 <sup>a</sup> , 0.34 <sup>a</sup> 2.77, 0.20; 2.94 <sup>a</sup> , 0.38 <sup>a</sup>

<sup>a</sup> DFT+U data with  $U_d(\text{Y}) = 12 \text{ eV}$  and  $J_d(\text{Y}) = 1 \text{ eV}$ ; <sup>b</sup> HSE06 calculations; <sup>c</sup> GW<sub>0</sub> calculations; <sup>d</sup> Experimental data; <sup>e</sup> DFT-LDA data; <sup>f</sup> DFT-GGA data

that the  $\text{Y}_2\text{O}_2\text{S}$  is a semiconductor with indirect bandgap, in agreement with past reports [7,16]. The  $\text{Y}_2\text{O}_2\text{S}$  valence band top is mainly of S-p and O-p orbitals, with some Y-d orbital contribution, whereas in the conduction band bottom the Y-d orbital dominates with some minor contributions from the O-p orbitals (**Fig. 4**). The valence band top becomes almost flat between the B and A points of the BZ, which is indicative of a heavy-hole band. Our DFT calculations show that the bandgap is 3.01 eV, which agrees with past reports from DFT calculations [7,15]. DFT underestimates the  $\text{Y}_2\text{O}_2\text{S}$  bandgap, which is experimentally detected between 4.6 and 4.8 eV, as explained in the introduction. Our HSE06 hybrid functional calculations, using the smaller 10-atom  $\text{Y}_2\text{O}_2\text{S}$  unit cell, showed a 3.94 eV bandgap at the  $\Gamma$  point, which is closer to the accepted experimental values. However, our GW<sub>0</sub> calculations showed a bandgap at the  $\Gamma$  point of 5.30 eV, which is an overestimation of the experimental bandgap. Additional calculations using the Bethe-Salpeter equation (BSE)[56], which accounts for the electron-hole interaction, showed an improved calculated bandgap of 5.08 eV. Although HSE06, GW<sub>0</sub>, and HSE are considered superior to DFT, they are impractical to be used for unit cells that contain more than a few atoms due to significant RAM requirements and CPU demand.

Our DFT+U calculations show an increased bandgap for the  $\text{Y}_2\text{O}_2\text{S}$  bandgap, which is in better agreement with experiments. However, this bandgap is now direct, in contrast with our DFT calculations and past reports. Therefore, the improvement on the  $\text{Y}_2\text{O}_2\text{S}$  bandgap by DFT+U is fortuitous. Kirchner-Hall et al. provided an extensive benchmark of the DFT+U bandgaps on several materials including oxysulfides, such as the  $\text{Y}_2\text{O}_2\text{S}$  [57]. The authors found that for d<sup>0</sup> elements, such as Y in the  $\text{Y}_2\text{O}_2\text{S}$ , DFT+U bandgaps are more sensitive to the projection methods used than the actual U value. Specifically, they found that for atomic localized functions, such as the ones used in this work, DFT+U fails to improve the bandgaps. Therefore, the DFT calculated band structure is sufficient for our analysis and a rigid scissor shift of about 1.6–1.8 eVs can be used to provide a band structure closer to the experimental one.

Doping with Er shows the Er 4f states at the Fermi energy region and splitting of the host bandgap to two smaller direct bandgaps. The Er doping and both bandgaps increase in an analogous relationship. DFT underestimates the width of the Er 4f band due to not correctly accounting for the partial localization of these electrons. The DOS calculations show that increased Er doping leads to more Er 4f states, which agrees with the increased light absorption observed experimentally [7]. However, the same calculations show no changes in the Y, S, and O orbitals due to doping (**Fig. 4**).

For the  $\text{Y}_2\text{O}_2\text{S}$  host, the Bader charge analysis shows charge transfers of 2.06 e per Y atom towards O and S atoms, which is in contrast from what is expected from the chemical formula. The O and S atom charges increase by 1.38 e per atom relative to their charges as isolated atoms. Calculated ion charges directly from VASP using projected localized orbitals [58] show similar results, as the above Bader calculated charges. Similarly, for the  $\text{Y}_2\text{O}_2\text{S}:\text{Er}^{+3}$  with 3.175% Er, the Bader charges show charge transfer of 1.58 e per Er atom and 1.62 e per Y atoms towards S and O atoms. In this case, the O and S atoms increase their per atom changes by about 1.14 e and 1.09 e, respectively. These results support that Er and Y form covalent bonds with S and O atoms in the yttrium oxysulfide structures.

#### 3.3. Optical properties experiments and calculations

##### 3.3.1. Experimental absorption spectra

**Fig. 5** shows the experimentally measured absorption spectra for  $\text{Y}_2\text{O}_2\text{S}:\text{Er}$  at 10% concentration. The absorption bands of the  $\text{Er}^{+3}$  ions correspond to transitions from the  $^4I_{15/2}$  ground state to various Er excited levels. Absorption bands were observed at 410 nm, 460 nm, 490 nm, 530 nm, 550 nm, 670 nm, 820 nm, 980 nm, and 1550 nm and are assigned to the  $\text{Er}^{+3}$  4f → 4f intraband transitions  $^4I_{15/2} \rightarrow ^4G$ ,  $^4F$ ,  $^2H_{9/2}$ ,  $^4I_{15/2} \rightarrow ^4F_{5/2}$ ,  $^4I_{15/2} \rightarrow ^4F_{7/2}$ ,  $^4I_{15/2} \rightarrow ^2H_{11/2}$ ,  $^4I_{15/2} \rightarrow ^4S_{3/2}$ ,  $^4I_{15/2} \rightarrow ^4F_{9/2}$ ,  $^4I_{15/2} \rightarrow ^4I_{9/2}$ ,  $^4I_{15/2} \rightarrow ^4I_{11/2}$ , and  $^4I_{15/2} \rightarrow ^4I_{13/2}$ , respectively.

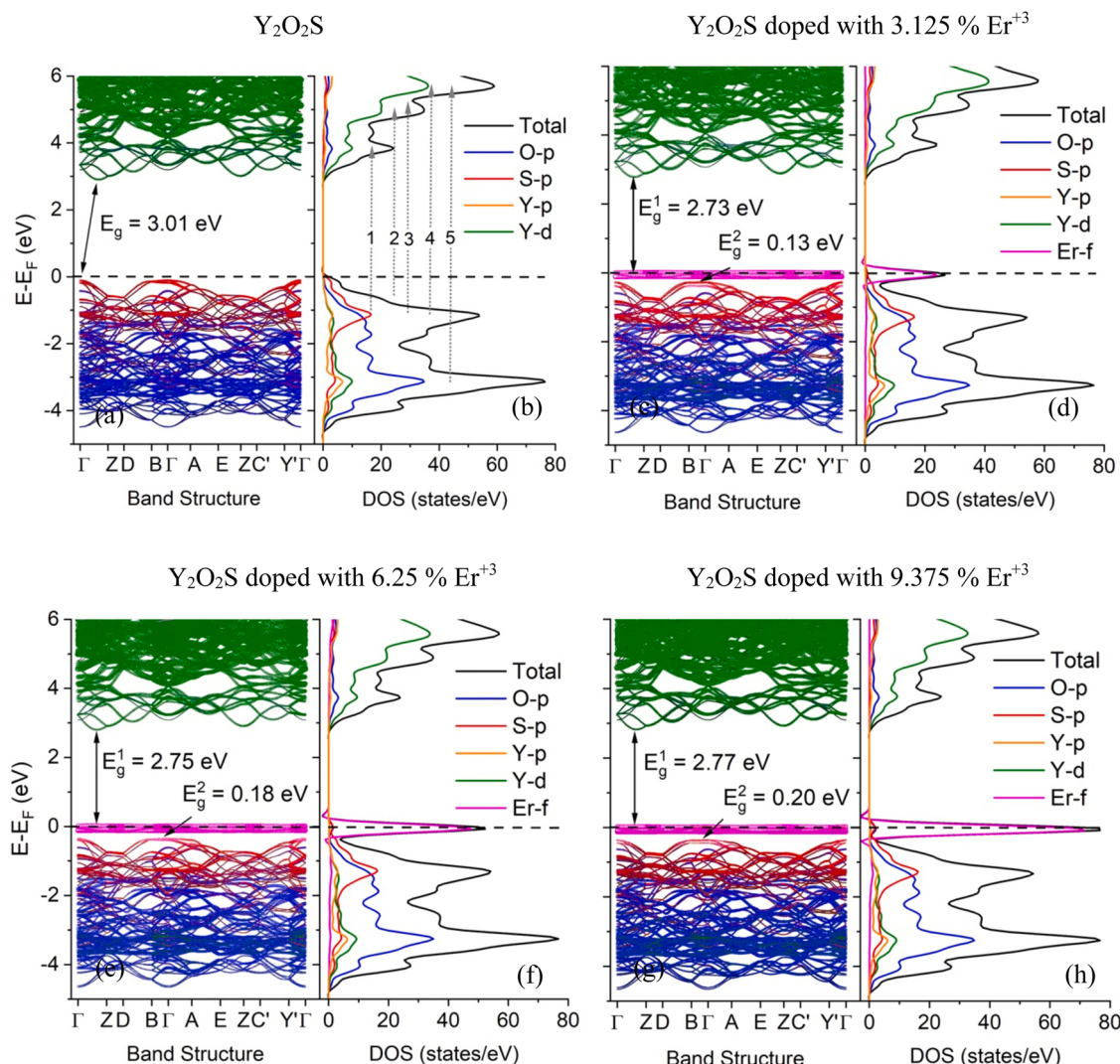


**Fig. 4.** Electronic band structure with orbital projections using the BZ path of Fig. 2 and corresponding total and projected DOS per orbital for  $\text{Y}_2\text{O}_2\text{S}$  ((a) and (b)) and doped  $\text{Y}_2\text{O}_2\text{S}$  with 3.125% Er ((c) and (d)), 6.25% Er ((e) and (f)), and 9.375% Er. Gray dotted arrows denote optical transitions. The dashed horizontal line is the Fermi energy ( $E_F$ ). The 80-atom unit cells were used.

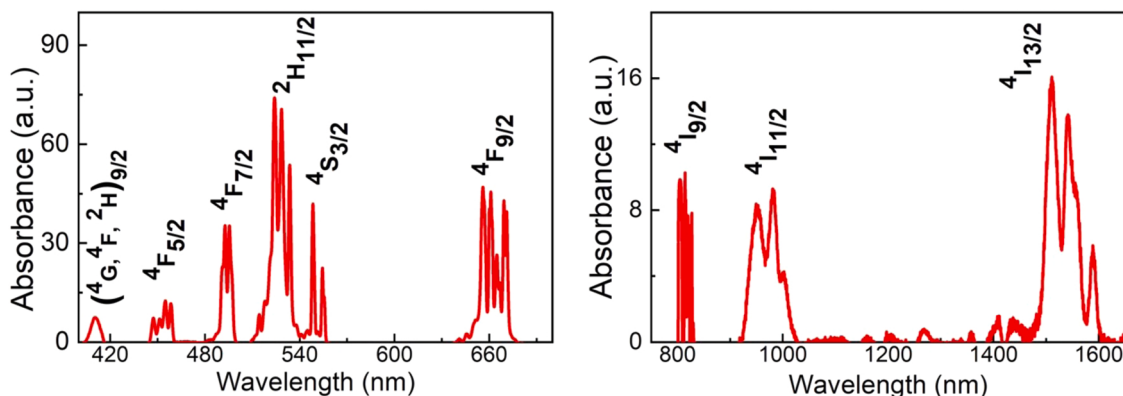


**Fig. 5.** Absorption spectra of  $\text{Y}_2\text{O}_2\text{S}: \text{Er}^{3+}$  at 10% Er concentration in a pallet form of powder. The assignment of the absorption spectra was based on previous publication [7].

The prepared material using two step synthesis method shows the typical  $\text{Er}^{3+}$  absorption spectra and agree with the data from the  $\text{Y}_2\text{O}_2\text{S}: \text{Er}^{3+}$  synthesized using the solid state method reported previously [7].

Fig. 5 shows that the highest absorbance is observed at 525 nm, whereas

the absorbance at the near infrared (i.e.,  $1.54 \mu\text{m}$ ) and around 411 nm and 453 nm are small. This shows that the Er doping causes transitions in the visible and the near infrared region.

### 3.3.2. Calculated optical properties for the host $\text{Y}_2\text{O}_2\text{S}$

**Fig. 6** shows the real and the imaginary part of the  $\text{Y}_2\text{O}_2\text{S}$  frequency-dependent dielectric function using the 10-atom unit cell, as well as its absorption coefficient  $\alpha$ , reflectivity  $R$ , and refractive index  $n$ . Here, we used the IPA, the RPA, and the  $\text{GW}_0+\text{RPA}$  method under the  $6 \times 6 \times 6$  BZ grid centered at the  $\Gamma$  point. We have also repeated the IPA and RPA calculations using the larger  $\Gamma$ -centered  $8 \times 8 \times 8$  grid (**Fig. S3**). **Table 2** shows the dielectric function maximum values and its locations in the energy spectrum for the imaginary part of the dielectric function, as well as the dielectric constant  $\epsilon_R(0)$  and the bandgap obtained from the onset of the  $\epsilon_I(\omega)$ , for all the structures of this work. The denser grid does not significantly shift the IPA and RPA calculated optical properties maximum values in the energy spectrum. However, the maximum of the imaginary part of the dielectric function appears smaller in the denser grid calculations (**Table 1**). The  $\text{GW}_0+\text{RPA}$  calculated frequency-dependent optical properties appears as energy shifted RPA calculations and are systematically lower than the corresponding properties calculated from the RPA and IPA, except for the absorption coefficient maxima. The results from the IPA are in a very good agreement with the RPA results up to about 20 eV. Therefore, for this work, we can safely use the IPA to calculate optical properties for the larger 80-atom unit cells. **Fig. 7** shows the dielectric function for the  $\text{Y}_2\text{O}_2\text{S}$  and its Er doped counterparts using the IPA method, whereas **Fig. 8** show their  $\alpha$ ,  $R$ , and  $n$ . **Figs. 6–8** and S2 show that there are analogous relationships between the imaginary part of dielectric function  $\epsilon_I(\omega)$  and the absorption coefficient  $\alpha(\omega)$  and the real part  $\epsilon_R(\omega)$  and the refractive index  $n(\omega)$ , respectively.

The  $\text{GW}_0+\text{RPA}$  shows that for the host  $\text{Y}_2\text{O}_2\text{S}$ ,  $n(\omega) \leq 1$  at about 13.2 eV, in agreement with the  $n(\omega)$  for wide-band semiconductors and insulators (**Figs. 6e, 8c**). The peaks in the  $\epsilon_I(\omega)$  denote transitions from the valence band to the conduction band, whereas the energy value at the onset of the  $\epsilon_I(\omega)$  is the bandgap. For the 80-atom unit cell, the  $\epsilon_I(\omega)$  onset for the  $\text{Y}_2\text{O}_2\text{S}$  is found at 3.26 eV, which is close to its bandgap value obtained from the band structure (**Fig. 4a**). For the IPA and RPA calculations, the bandgap values obtained from the  $\epsilon_I(\omega)$  onsets are slightly larger than the corresponding values from the band structure calculations, whereas the opposite is found for the  $\text{GW}_0+\text{RPA}$ . Our calculations show that the host  $\text{Y}_2\text{O}_2\text{S}$  has no absorption peaks in the visible ( $\sim 1.8$ – $3.0$  eV), in agreement with past reports [14,15].

For the 80-atom  $\text{Y}_2\text{O}_2\text{S}$  unit cell, the  $\epsilon_I(\omega)$  highest peak is found at

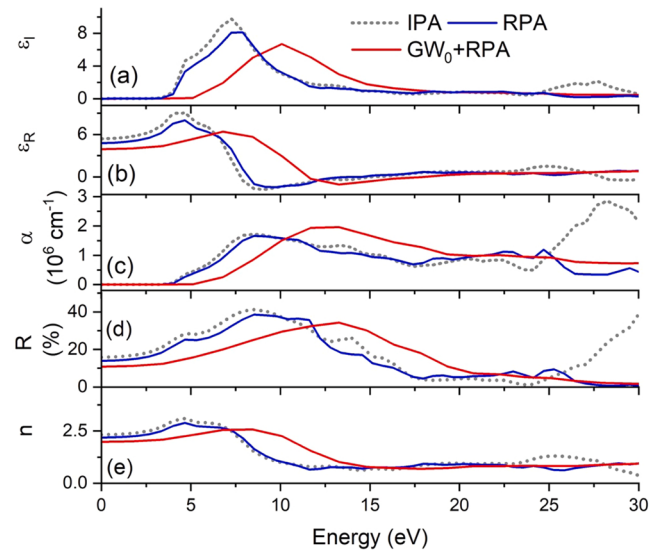


**Fig. 6.** (a) The real ( $\epsilon_R$ ) and the imaginary ( $\epsilon_I$ ) part of the frequency-dependent dielectric function for  $\text{Y}_2\text{O}_2\text{S}$  as a function of energy using the IPA, RPA, and  $\text{GW}_0+\text{RPA}$ , (b) the absorption coefficient  $\alpha$ , (c) the reflectivity  $R$ , and (d) the refractive index  $n$ . The 10-atom  $\text{Y}_2\text{O}_2\text{S}$  unit cell were used.

**Table 2**

The real and the imaginary dielectric function static ( $\epsilon_R(0)$  and  $\epsilon_I(0)$ ) and maximum values ( $\epsilon_R(\omega)_{max}$  and  $\epsilon_I(\omega)_{max}$ ) and the energy value of the  $\epsilon_I(\omega)$  onset, per method and unit cell configuration used. The energy locations of the  $\epsilon_I(\omega)_{max}$  are given in parentheses. Values in square brackets refer to the calculations using the  $\Gamma$ -centered  $8 \times 8 \times 8$  grid.

Property	Material & Method					
	$\text{Y}_2\text{O}_2\text{S}$		$\text{Y}_2\text{O}_2\text{S}:\text{Er}^{+3}$			
	IPA	RPA	$\text{GW}_0$ +RPA	3.175% Er	6.25% Er	9.375% Er
$\epsilon_R(0)^{3,4}$	5.49 [5.47] <sup>1</sup>	4.84 [4.79] <sup>1</sup>	3.94 <sup>1</sup>			
$\epsilon_R(\omega)_{max}$	5.25 <sup>2</sup> 9.08 [8.74] <sup>1</sup>	7.83 [7.82] <sup>1</sup>	6.44 <sup>1</sup>	11.93	21.15	37.86
$\epsilon_I(\omega)_{max}$	10.23 <sup>2</sup> 9.77 [9.28]	8.07 [7.75]	6.81	10.07	9.91	9.74
( $\omega$ )	(7.28; [7.26]) <sup>1</sup>	(7.28; 7.90)	(10.08)			
( $\omega$ )	10.82 <sup>2</sup> (6.91) <sup>2</sup>			10.64	10.46	10.56
Onset	3.40 [3.43]		5.14	(6.94)	(7.01)	(7.02)
$\epsilon_I(\omega)^{5,6}$		3.32 <sup>2</sup>				

<sup>1</sup>10 atom unit cell; <sup>2</sup> 80 atom unit cell; <sup>3</sup> experimental value 4.67 for  $\text{La}_2\text{O}_2\text{S}$  from Ref. [4,14] calculated value of 5.3 from Ref. [5,15] experimental value 5.00 from Ref. [14]; calculated value 3.00 from Ref. [14].

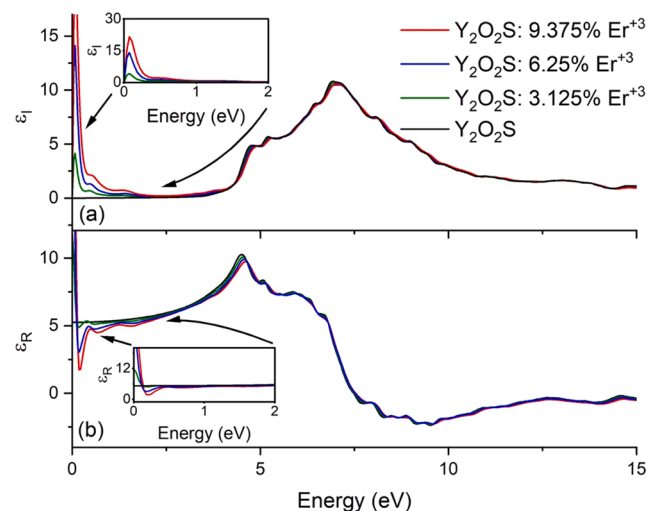


**Fig. 7.** (a) The imaginary part of the frequency-dependent dielectric function ( $\epsilon_I$ ) using the IPA for the host  $\text{Y}_2\text{O}_2\text{S}$  and its  $\text{Er}^{+3}$  doped counterparts and (b) the real part ( $\epsilon_R$ ).

6.91 eV, whereas three other peaks are found at 4.74 eV, 5.20 eV, and 6.42 eV. The calculations using the smaller unit cell show the  $\epsilon_I(\omega)$  highest peak at 7.24–7.26 eV using the IPA method, with the RPA calculations showing the same maximum value also at 7.91–7.92 eV. The  $\epsilon_I(\omega)$  highest peak using the  $\text{GW}_0+\text{RPA}$  method is found at 10.08 eV, which is blue shifted by about 2.8 eV relative to the IPA calculations. Our IPA and RPA results are in excellent agreement with the past calculations by Li and Ahuja, who found  $\text{Y}_2\text{O}_2\text{S}$   $\epsilon_I(\omega)$  peaks at 4.65 eV, 5.16 eV, and 7.1 eV, the last being the maximum for  $\epsilon_I(\omega)$ . Experimentally, the maximum  $\epsilon_I(\omega)$  was found at 6.1 eV followed by a peak at 7.7 eV of less  $\epsilon_I(\omega)$  [14]. Since the DFT calculated bandgap differs from

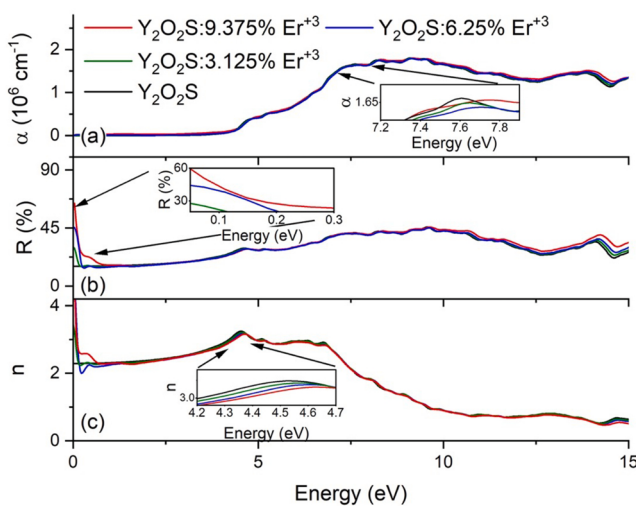


**Fig. 8.** (a) The absorption coefficient  $\alpha$  as a function of energy using the IPA method for undoped  $\text{Y}_2\text{O}_2\text{S}$  and its Er doped counterparts, (b) the reflectivity  $R$ , and (c) the refractive index  $n$ .

the experimentally observed bandgap by 1.6–1.8 eV, applying this rigid shift to the above values provides a good agreement of the IPA calculations, using the 80-atom unit cell, with the experimental data. Interestingly, the  $\text{GW}_0+\text{RPA}$   $\varepsilon_I(\omega)$  peaks are blue shifted relative to experiments.

Li and Ahuja assigned their first  $\varepsilon_I(\omega)$  peak at 4.65 eV to the  $\text{Y}-4\text{p}\rightarrow\text{Y}-4\text{d}$  transition, whereas Itoh and Inabe assigned their corresponding first  $\varepsilon_I(\omega)$  peak to the  $\text{S}-3\text{p}\rightarrow\text{Y}-4\text{d}$  transition. Our DOS calculations show an S 3p peak at about 1.13 eV below the Fermi energy, which overlaps with a significantly smaller peak of Y 4p. Our  $\varepsilon_I(\omega)$  peak at 4.8 eV is assigned to transition 1 in Fig. 4b. Similarly, the other three  $\varepsilon_I(\omega)$  peaks located at 5.20 eV, 6.42 eV, and 6.94 eV are assigned to transitions 2, 3, and 4 respectively.

The real part of the dielectric function describes the material's polarization and is used to calculate the static dielectric constant  $\varepsilon_R(0)$ . Table 2 shows that the RPA calculations for the 10-atom unit cell and the IPA calculation for the 80-atom unit cells provide  $\varepsilon_R(0)$  values closer to the experimentally reported value. Our  $\text{GW}_0+\text{RPA}$  calculations underestimate  $\varepsilon_R(0)$  in contrast to the IPA and RPA calculations. The absorption coefficient  $a$  is close to zero in the visible and the infrared part of the spectrum for all materials of this work. There is a relationship between  $a$ ,  $R$ , and transmitted light  $T$  as  $T = (1 - R)^2 \exp(-ad)/[(1 - R^2 \exp(-2ad)]$ , where  $d$  is the distance light travels in the material [59]. Thus, in the case of  $a \approx 0$ , and  $R$  alone is sufficient for estimating the amount of light transmitted. For the host  $\text{Y}_2\text{O}_2\text{S}$ , the absorption coefficient is at maximum at 8.50–9.07 eV for the IPA and RPA and 11.66 eV for the  $\text{GW}_0+\text{RPA}$  ( $\omega \leq 20$  eV). Scafetta et al. stated that maximum peaks in the absorption coefficient spectrum correspond to a transition from a valance band of maximum DOS to a conduction band of also maximum DOS [60]. In this case, this is the  $\text{O}-2\text{p}\rightarrow\text{Y}-4\text{d}$ , and is shown as transition 4 in Fig. 4a.

The host  $\text{Y}_2\text{O}_2\text{S}$  static reflectivity  $R$  is 10.87–16.03% for all methods and unit cells of this work, with the lower end value corresponding to the  $\text{GW}_0+\text{RPA}$  calculations. Reflectivity increases to a maximum of 34.39–45.84% for the IPA and RPA calculations. As expected, the host  $\text{Y}_2\text{O}_2\text{S}$  is not a good candidate as a mirror-type coating material. The refractive index  $n$  for the host  $\text{Y}_2\text{O}_2\text{S}$  starts at 1.98–2.33 and is maximized to 2.85–3.26, with the larger energy referring to the  $\text{GW}_0+\text{RPA}$  calculations. As stated above, the refractive index becomes less than 1 at energies expected from wide-band semiconductors and insulators.

### 3.3.3. Optical properties calculations for the $\text{Y}_2\text{O}_2\text{S}:\text{Er}^{3+}$ doped configurations

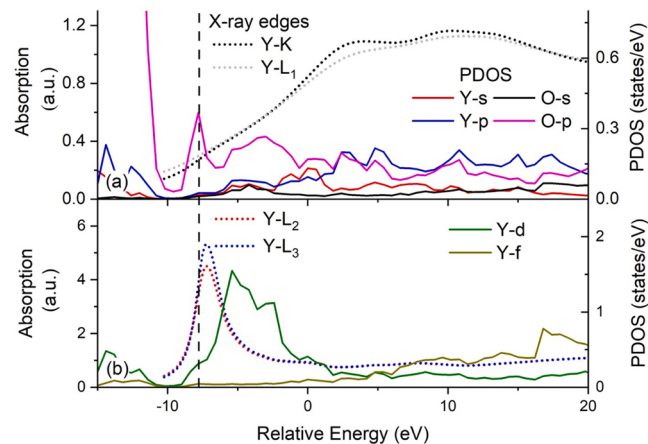
Figs. 7 and 8 show that doping Y with Er atoms in the  $\text{Y}_2\text{O}_2\text{S}$  has minimal effects in the optical properties except in the energy region below the bandgap. The  $\varepsilon_I(\omega)$  for the doped configurations show peaks at 1.37 eV, 0.50 eV, and 0.07 eV (Fig. 7a) in order of increasing intensity  $\varepsilon_I(\omega)$ . There is an analogous relationship between the  $\varepsilon_I(\omega)$  intensities of these peaks and the Er doping. The above energies are transformed to the wavelengths 418 nm, 590 nm, and 742 eV, respectively, by applying a rigid energy shift of about 1.6 eV. Therefore, we can assign these peaks to the closest peak in our experimental absorption spectra (Fig. 5) as follows: The 1.37 eV peak corresponds to the low intensity peaks of 400 nm and 450 nm, the 0.50 eV peak to the high intensity 525 nm peak, and the 0.07 eV to the peaks at 650 nm or 800 nm. Recall that the imaginary part of the frequency-dependent dielectric function of the host  $\text{Y}_2\text{O}_2\text{S}$  shows no peaks before the  $\varepsilon_I(\omega)$  onset. Therefore, these transitions do not involve the conduction band and are intraband transitions within the Er 4f band. Table 2 shows that the static dielectric constant  $\varepsilon_R(0)$  is increased with increased Er doping, which is indicative of an improved dielectric material.

Fig. 8 shows that the static reflectivity  $R(0)$  increases along with increased Er doping, reaching a value of 54.86% for 9.375% Er doping. We found that  $R(\omega)$  increases in the bandgap energy region, for energies below the plasma frequencies  $\omega_p$ . Our VASP calculated plasma frequencies  $\omega_p$  are 0.17 eV, 0.26 eV, and 0.34 eV for Er doping of 3.175%, 6.25%, and 9.375%, respectively. Since increased reflectivity reduces light transmission, we expect that the transmitted light intensity, which corresponds to the 0.07 eV peak to be very small. This agrees with our experimental absorption spectra and past reports that show that the near infrared Er emission is small.

### 3.4. Simulated XANES on Y and Er edges

XANES provides information about the geometry around the probed atom and electronic information for the states above the Fermi level. Figs. 9 and 10 show the FEFF calculated XANES spectra at the Y K-, L<sub>1</sub>-, L<sub>2</sub>-, and L<sub>3</sub>-edges and at the Er M<sub>5</sub>-edge, respectively together with the projected DOS per orbital (PDOS).

The PDOS is used to assign transitions at the edge and pre-edge regions [61,62]. At the x-ray edge, the absorption shows a first sharp rise, which is found in the literature as the “white line” and corresponds to transitions from filled states to states in the continuum. Selection rules



**Fig. 9.** (a) The Y K- and L<sub>1</sub>-edge XANES spectra for the  $\text{Y}_2\text{O}_2\text{S}$  showing the normalized absorption (left y-axis) with respect to the energy relative to the ionization energy and projected DOS (PDOS) per Y and O s and p orbitals (right y-axis), as calculated by FEFF 10 and (b) the Y L<sub>2</sub>- and L<sub>3</sub>-edge XANES spectra (left y-axis) and the projected DOS per Y d and f orbitals (right y-axis). The vertical dashed line is the Fermi energy at  $-7.819$  eV.

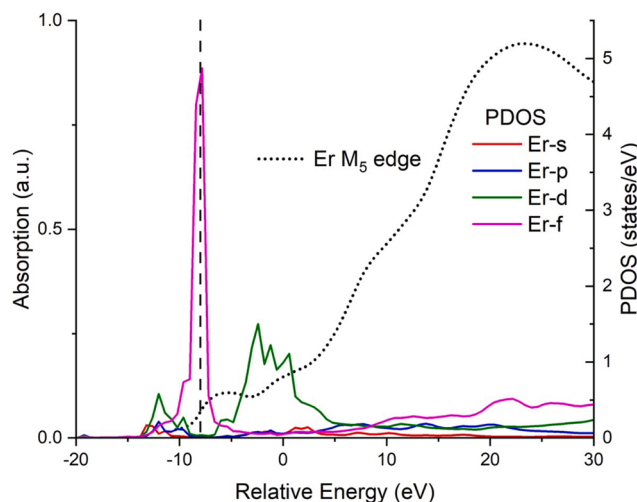


**Fig. 10.** The Er  $M_5$ -edge XANES spectra of the  $Y_2O_2S:Er^{+3}$  with 9.375% doping showing the normalized absorption (left y-axis) with respect to the energy relative to the ionization energy and projected DOS per Er orbital (right y-axis), as calculated by FEFF 10. The vertical dashed line is the Fermi energy at  $-7.943$  eV. The DOS has been red shifted so that the Fermi energy coincides with the peak of the Er 4f band.

dicate that  $\Delta l = l_f - l_i \neq 0$ , where  $l_f$  and  $l_i$  are angular momenta quantum numbers for the initial and final states, respectively. Therefore, the white lines at the K- and L<sub>1</sub>-edges denote transitions from the 1s and 2s states, respectively to a p state in the continuum, whereas the L<sub>2</sub> and L<sub>3</sub> white lines denote transitions from a 2p state to a d state in the continuum, respectively. Similarly, the M<sub>5</sub>-edge white line denotes a transition from a 3d state to an f state in the continuum. The FEFF calculated Fermi energies for the host  $Y_2O_2S$  and the  $Y_2O_2S:Er^{+3}$  with 9.375% doping are  $-7.819$  eV and  $-7.943$  eV, respectively. These values are close to the VASP calculated values  $-7.070$  eV and  $-6.974$  eV, respectively. However, the FEFF calculated absorption spectra data are typically shifted in energy due to broadening [61]. The FEFF calculated valance band top PDOS are red shifted since the Fermi energy appears after the bandgap (Fig. 10). The Y s, Y p, and O p DOS peaks below the Y K- and L<sub>1</sub>-edges reveal the final state in the continuum for both edges (Fig. 9a). Similarly, for both Y L<sub>2</sub>- and L<sub>3</sub>-edges, the final state is the Y-d state (Fig. 9b).

Pre-edge peaks denote transitions to bound states in the conduction band. Mao et al., observed no pre-edge feature in the Y K- and Er L-edges for Er doped yttrium oxide nanotubes. However, the XANES spectra at our Er M<sub>5</sub>-edge show several pre-edge features. Our focus is on the pre-edge broad shoulder of about 4 eV width in the vicinity of the Er 4f band and centered at around  $-7$  eV (Fig. 10). The width of this shoulder is about the same as the width of the Er 4f band. This peak is not associated with the Er d-band, which is significantly broader ( $\sim 8\text{--}9$  eV width). Therefore, the presence of the pre-edge broad shoulder at  $-7$  eV could be related to transitions within the Er 4f band. Moreover, we found no changes in the Er M<sub>5</sub>-edge due to increased doping.

#### 4. Conclusions

We used computational methods to analyze the band structure and the optical properties of  $Y_2O_2S$  and its  $Er^{+3}$  doped counterparts at various Er concentrations. We also collected  $Y_2O_2S:Er^{+3}$  absorption spectra experimentally, which show light emission in the visible and near infrared, as expected. This light emission is attributed to Er f-f intraband transitions. DFT shows that the  $Y_2O_2S$  is a wide band semiconductor with an indirect bandgap, in agreement with past reports. Our DFT calculated bandgap is 1.6–1.8 eV smaller than what is expected by experiments. Our HSE06,  $GW_0$ , and the BSE calculations improve the

DFT calculated bandgap, with the latter to show the best agreement with the experiments. The bandgap improvement by the DFT+U calculations is fortuitous, and it alters the conduction band structure. The  $Er^{+3}$  doping on  $Y_2O_2S$  causes the split of the  $Y_2O_2S$  bandgap to two smaller bandgaps, with the Er 4f orbitals to be located at the Fermi energy region. Therefore, the  $Y_2O_2S:Er^{+3}$  have semi-metallic properties. The DOS calculations and the Bader charge calculations show that Y(Er)-O and Y(Er)-S are covalent bonds.

The dielectric function and other optical properties were calculated using the IPA, for all configurations of this work. Additionally, the RPA and the many-body  $GW_0+RPA$  have been also used for the optical calculations for the host  $Y_2O_2S$  and showed that the IPA provides reliable information for energies up to about 20 eV. The imaginary part of the dielectric function showed that the host  $Y_2O_2S$  has no transitions in the visible. For the  $Y_2O_2S:Er^{+3}$  cases, the imaginary part of the frequency-dependent dielectric function revealed three peaks in the bandgap energy region, which correspond to Er f-f intraband transitions. These transitions are in direct correspondence with our absorption experimental data, by applying an energy rigid shift of about 1.6 eV. Reflectivity calculations show that the transition that corresponds to the lowest energy is suppressed, in agreement with our experimental absorption measurement. Moreover, XANES calculations at the Er M<sub>5</sub>-edge show a peak at the pre-edge region in the proximity of the Er 4f band, which is indicative of the Er f-f intraband transitions.

#### CRediT authorship contribution statement

**Nicholas Dimakis:** Conceptualization, Methodology, Supervision, Validation, Writing – review & editing. **Eric Baldemar Rodriguez Jr.:** Data curation, Validation, Investigation. **Kofi Nketia Ackaah-Gyasi:** Data curation, Validation, Investigation. **Madhab Pokhrel:** Conceptualization, Methodology, Writing – review & editing, Data curation, Validation.

#### Declaration of Competing Interest

The authors declare the following financial interests/personal relationships which may be considered as potential competing interests, Nicholas Dimakis reports financial support was provided by The University of Texas Rio Grande Valley. Eric Baldemar Rodriguez Jr. reports financial support was provided by The University of Texas Rio Grande Valley.

#### Data Availability

The raw and proceeded data required to reproduce these findings are available to download from <https://data.mendeley.com/drafts/bym3yj3xxc>.

#### Acknowledgements

The author(s) would like to acknowledge funding provided by the National Science Foundation CREST Center for Multidisciplinary Research Excellence in Cyber-Physical Infrastructure Systems (NSF Award No. 2112650). The opinions expressed in this paper (or thesis or report or dissertation) are solely those of the author(s), and do not necessarily represent those of the NSF. The authors also acknowledge the Texas Advanced Computing Center (TACC) at The University of Texas at Austin for providing HPC resources that have contributed to the research results reported within this paper. URL: <http://www.tacc.utexas.edu>.

#### Appendix A. Supporting information

Supplementary data associated with this article can be found in the online version at doi:[10.1016/j.mtcomm.2022.104328](https://doi.org/10.1016/j.mtcomm.2022.104328).

## References

- [1] Y. Kawahara, V. Petrykin, T. Ichihara, N. Kijima, M. Kakihana, Synthesis of high-brightness sub-micrometer  $\text{Y}_2\text{O}_2\text{S}$  red phosphor powders by complex homogeneous precipitation method, *Chem. Mat.* 18 (2006) 6303–6307.
- [2] L. Ozawa, Application of Cathodoluminescence to Display Devices, Alcuin Books and Autographs, LLC, Tokyo, 1994.
- [3] T. Jüstel, H. Nikol, C. Ronda, New developments in the field of luminescent materials for lighting and displays, *Angew. Chem. Int. Ed.* 37 (1998) 3084–3103.
- [4] S. Yuan, Y. Yang, B. Fang, G. Chen, Effects of doping ions on afterglow properties of  $\text{Y}_2\text{O}_2\text{S}$ :Eu phosphors, *Opt. Mater.* 30 (2007) 535–538.
- [5] P.-F. Ai, Y.-L. Liu, L.-Y. Xiao, H.-J. Wang, J.-X. Meng, Synthesis of  $\text{Y}_2\text{O}_2\text{S}:\text{Eu}^{3+}, \text{Mg}^2+$ ,  $\text{Ti}^{4+}$  hollow microspheres via homogeneous precipitation route, *Sci. Technol. Adv. Mater.* 11 (2010), 035002-035002.
- [6] C. Guo, L. Luan, C. Chen, D. Huang, Q. Su, Preparation of  $\text{Y}_2\text{O}_2\text{S}:\text{Eu}^{3+}$  phosphors by a novel decomposition method, *Mater. Lett.* 62 (2008) 600–602.
- [7] M. Pokhrel, G.A. Kumar, C.G. Ma, M.G. Brik, B.W. Langloss, I.N. Stanton, M. J. Therien, D.K. Sardar, Y. Mao, Electronic and optical properties of Er-doped  $\text{Y}_2\text{O}_2\text{S}$  phosphors, *J. Mater. Chem. C* 3 (2015) 11486–11496.
- [8] G.F.J. Garlick, C.L. Richards, Multiphoton excitation of visible emission in  $\text{Y}_2\text{O}_2\text{S}$ :Er, Yb phosphors by 810 nm excitation, *J. Lumin.* 9 (1974) 424–431.
- [9] C.-C. Kang, R.-S. Liu, J.-C. Chang, B.-J. Lee, Synthesis and luminescent properties of a new yellowish-orange afterglow phosphor  $\text{Y}_2\text{O}_2\text{S}:\text{Ti}, \text{Mg}$ , *Chem. Mat.* 15 (2003) 3966–3968.
- [10] T. Hoshina, Unpublished, 1983.
- [11] C.W. Struck, W.H. Fonger, Dissociation of  $\text{Eu}^{+3}$  charge-transfer state in  $\text{Y}_2\text{O}_2\text{S}$  and  $\text{La}_2\text{O}_2\text{S}$  into  $\text{Eu}^{+2}$  and a free hole, *Phys. Rev. B* 4 (1971) 22–34.
- [12] M. Mikami, A. Oshiyama, First-principles band-structure calculation of yttrium oxysulfide, *Phys. Rev. B* 57 (1998) 8939–8944.
- [13] Y. Fu, W. Cao, Y. Peng, X. Luo, M. Xing, The upconversion luminescence properties of the  $\text{Yb}^{3+}-\text{Ho}^{3+}$  system in nanocrystalline  $\text{Y}_2\text{O}_2\text{S}$ , *J. Mater. Sci.* 45 (2010) 6556–6561.
- [14] M. Itoh, Y. Inabe, Optical properties and electronic structure of yttrium oxysulfide, *Phys. Rev. B* 68 (2003), 035107.
- [15] S. Li, R. Ahuja, Electronic, elastic, and optical properties of  $\text{Y}_2\text{O}_2\text{S}$ , *J. Appl. Phys.* 97 (2005), 103711.
- [16] B. Qu, J. Wang, K. Liu, R. Zhou, L. Wang, A comprehensive study of the red persistent luminescence mechanism of  $\text{Y}_2\text{O}_2\text{S}:\text{Eu}, \text{Ti}, \text{Mg}$ , *Phys. Chem. Chem. Phys.* 21 (2019) 25118–25125.
- [17] M. Mikami, S. Nakamura, M. Itoh, K. Nakajima, T. Shishido, Lattice dynamics and dielectric properties of yttrium oxysulfide, *Phys. Rev. B* 65 (2002), 094302.
- [18] P.P. Sukul, K. Kumar, H. Swart, Erbium energy bridging upconversion mechanism studies on BAKL: $\text{Er}^{3+}/\text{Yb}^{3+}$  glass-ceramics and simultaneous enhancement of color purity of the green luminescence, *Dalton Trans.* 51 (2022) 2827–2839.
- [19] J.M. Zavada, M. Thaik, U. Hömmerich, J.D. MacKenzie, C.R. Abernathy, F. Ren, H. Shen, J. Pamulapati, H. Jiang, J. Lin, R.G. Wilson, Luminescence from erbium-doped gallium nitride thin films, *MRS Internet J. Nitride Semicond. Res.* 4 (1999) 926–932.
- [20] F. Auzel, Upconversion and anti-stokes processes with f and d ions in solids, *Chem. Rev.* 104 (2004) 139–174.
- [21] S. Buddhudu, F.J. Bryant, Optical transitions of  $\text{Er}^{3+}:\text{La}_2\text{O}_2\text{S}$  and  $\text{Er}^{3+}:\text{Y}_2\text{O}_2\text{S}$ , *J. Less Common Met.* 147 (1989) 213–225.
- [22] P. Hohenberg, W. Kohn, Inhomogeneous electron gas, *Phys. Rev.* 136 (1964) B864–B871.
- [23] W. Kohn, L.J. Sham, Self-consistent equations including exchange and correlation effects, *Phys. Rev.* 140 (1965) A1133–A1138.
- [24] J.J. Rehr, A.L. Ankudinov, Progress in the theory and interpretation of XANES, *Coord. Chem. Rev.* 249 (2005) 131–140.
- [25] A.I. Liechtenstein, V.I. Anisimov, J. Zaanen, Density-functional theory and strong interactions: orbital ordering in Mott-Hubbard insulators, *Phys. Rev. B* 52 (1995) R5467–R5470.
- [26] J. Heyd, G.E. Scuseria, M. Ernzerhof, Hybrid functionals based on a screened Coulomb potential, *J. Chem. Phys.* 118 (2003) 8207–8215.
- [27] M. Shishkin, G. Kresse, Implementation and performance of the frequency-dependent GW method within the PAW framework, *Phys. Rev. B* 74 (2006), 035101.
- [28] F. Aryasetiawan, O. Gunnarsson, The GW method, *Rep. Prog. Phys.* 61 (1998) 237–312.
- [29] W.G. Aulbur, L. Jönsson, J.W. Wilkins, Quasiparticle calculations in solids, *J. Phys. C Solid State Phys.* 54 (2000) 1–218.
- [30] S.L. Adler, Quantum theory of the dielectric constant in real solids, *Phys. Rev.* 126 (1962) 413–420.
- [31] N. Wiser, Dielectric constant with local field effects included, *Phys. Rev.* 129 (1963) 62–69.
- [32] H. Ehrenreich, M.H. Cohen, Self-consistent field approach to the many-electron problem, *Phys. Rev.* 115 (1959) 786–790.
- [33] M. Pokhrel, N. Ray, G. Kumar, D. Sardar, Comparative studies of the spectroscopic properties of  $\text{Nd}^{3+}:\text{YAG}$  nanocrystals, transparent ceramic and single crystal, *Opt. Mater. Express* 2 (2012) 235–249.
- [34] L. Han, M. Pan, Y. Lv, Y. Gu, X. Wang, D. Li, Q. Kong, X. Dong, Fabrication of  $\text{Y}_2\text{O}_2\text{S}:\text{Eu}^{3+}$  hollow nanofibers by sulfurization of  $\text{Y}_2\text{O}_3:\text{Eu}^{3+}$  hollow nanofibers, *Journal of Materials Science: Materials in Electronics*, 26, 2015, 677–684.
- [35] K. Jorissen, J.J. Rehr, Calculations of electron energy loss and x-ray absorption spectra in periodic systems without a supercell, *Phys. Rev. B* 81 (2010), 245124.
- [36] G. Kresse, J. Hafner, Ab initio molecular dynamics for liquid metals, *Phys. Rev. B* 47 (1993) 558(R)–561(R).
- [37] G. Kresse, J. Hafner, Ab initio molecular-dynamics simulation of the liquid-metal–amorphous–semiconductor transition in germanium, *Phys. Rev. B* 49 (1994) 14251–14269.
- [38] G. Kresse, J. Furthmüller, Efficiency of ab-initio total energy calculations for metals and semiconductors using a plane-wave basis set, *Comput. Mater. Sci.* 6 (1996) 15–50.
- [39] G. Kresse, J. Furthmüller, Efficient iterative schemes for ab initio total-energy calculations using a plane-wave basis set, *Phys. Rev. B Condens. Matter* 54 (1996) 11169–11186.
- [40] P.E. Blöchl, Projector augmented-wave method, *Phys. Rev. B* 50 (1994) 17953–17979.
- [41] G. Kresse, D. Joubert, From ultrasoft pseudopotentials to the projector augmented-wave method, *Phys. Rev. B* 59 (1999) 1758–1775.
- [42] J.P. Perdew, K. Burke, M. Ernzerhof, Generalized gradient approximation made simple, *Phys. Rev. Lett.* 77 (1996) 3865–3868.
- [43] S. Grimme, J. Antony, S. Ehrlich, H. Krieg, A consistent and accurate ab initio parametrization of density functional dispersion correction (DFT-D) for the 94 elements H–Pu, *J. Chem. Phys.* 132 (2010) 154104–154118.
- [44] H.J. Monkhorst, J.D. Pack, Special points for Brillouin-zone integrations, *Phys. Rev. B* 13 (1976) 5188–5192.
- [45] W. Tang, E. Sanville, G. Henkelman, A grid-based Bader analysis algorithm without lattice bias, *J. Phys. Condens. Matter* 21 (2009), 084204.
- [46] E. Sanville, S.D. Kenny, R. Smith, G. Henkelman, Improved grid-based algorithm for Bader charge allocation, *J. Comput. Chem.* 28 (2007) 899–908.
- [47] G. Henkelman, A. Arnaldsson, H. Jónsson, A fast and robust algorithm for Bader decomposition of charge density, *Comput. Mater. Sci.* 36 (2006) 354–360.
- [48] M. Yu, D.R. Trinkle, Accurate and efficient algorithm for Bader charge integration, *J. Chem. Phys.* 134 (2011), 064111.
- [49] R.F.W. Bader, Atoms in Molecules. Encyclopedia of Computational Chemistry, John Wiley and Sons, 1998.
- [50] M. Gajdoš, K. Hummer, G. Kresse, J. Furthmüller, F. Bechstedt, Linear optical properties in the projector-augmented wave methodology, *Phys. Rev. B* 73 (2006), 045112.
- [51] J.J. Kas, F.D. Vila, C.D. Pemmaraju, T.S. Tan, J.J. Rehr, Advanced calculations of X-ray spectroscopies with FEFF10 and Corvus, *J. Synchrotron, Rad* 28 (2021) 1801–1810.
- [52] J.J. Rehr, J.J. Kas, M.P. Prange, A.P. Sorini, Y. Takimoto, F. Vila, Ab initio theory and calculations of X-ray spectra, *Comptes Rendus Phys.* 10 (2009) 548–559.
- [53] J.J. Rehr, R.C. Albers, Theoretical approaches to x-ray absorption fine structure, *Rev. Mod. Phys.* 72 (2000) 621–654.
- [54] L. Hedin, B.I. Lundqvist, Explicit local exchange-correlation potentials, *J. Phys. C Solid State Phys.* 4 (1971) 2064–2083.
- [55] R.N. Bhattacharya, C.Y. Lee, F.H. Pollak, D.M. Schleich, Optical study of amorphous  $\text{MoS}_3$ : Determination of the fundamental energy gap, *J. Non-Cryst. Solids* 91 (1987) 235–242.
- [56] E.E. Salpeter, H.A. Bethe, A. Relativistic, Equation for bound-state problems, *Phys. Rev.* 84 (1951) 1232–1242.
- [57] N.E. Kirchner-Hall, W. Zhao, Y. Xiong, I. Timrov, I. Dabo, Extensive benchmarking of DFT+U calculations for predicting band gaps, *Appl. Sci.* 11 (2021) 2395.
- [58] M. Schüler, O.E. Peil, G.J. Krabberger, R. Pordzik, M. Marsman, G. Kresse, T. O. Wehling, M. Aichhorn, Charge self-consistent many-body corrections using optimized projected localized orbitals, *J. Phys. Condens. Matter* 30 (2018) 475901–475910.
- [59] D.C. Look, J.H. Leach, On the accurate determination of absorption coefficient from reflectance and transmittance measurements: application to Fe-doped GaN, *J. Vac. Sci. Technol. B* 34 (2016) 04J105.
- [60] M.D. Scafetta, A.M. Cordi, J.M. Rondinelli, S.J. May, Band structure and optical transitions in  $\text{LaFeO}_3$ : theory and experiment, *J. Phys. Condens. Matter* 26 (2014), 505502.
- [61] H. Asakura, T. Shishido, K. Teramura, T. Tanaka, A theoretical approach to La L<sub>1</sub>-edge XANES spectra of La complex oxides and their local configuration, *J. Chem. Phys.* 142 (2015), 164507.
- [62] S. Limpijumpong, S. Rujirawat, A. Boonchun, M.F. Smith, B. Cherdhirunkorn, Identification of Mn site in  $\text{Pb}(\text{Zr}, \text{Ti})\text{O}_3$  by synchrotron x-ray absorption near-edge structure: theory and experiment, *Appl. Phys. Lett.* 90 (2007), 103113.